Low Temperature Synthesis of Large-Size Anatase TiO$_2$ Nanosheets with Enhanced Photocatalytic Activities

Xiao Tang,* Wanyi Chu, Jueshi Qian, Jingcheng Lin, and Guozhong Cao*

TiO$_2$ nanosheets have continuously been intriguing due to their high surface activities as photocatalyst but still challenging to synthesis large-scale 2D nanostructures. A special microstructure evolution of TiO$_2$, ripening in aqueous solution at low temperature (≈4 °C), is found for the first time, i.e., from the initial aperiodic atom-networks gradually into low crystallized continuous spongy structure with small crystal facets and ultimately forming large-size anatase nanosheets with exposed (101) and (200) facets. Based on this finding, the synthesized anatase TiO$_2$ nanosheets possess monodispersed large-scale 2D nanostructure so as to exhibit appreciable quantum size effects and remarkable enhanced optical absorption capacity. Using photocatalytic reduction of Cr (VI) to Cr (III) as the probe reaction to evaluate photocatalytic activities of the TiO$_2$ nanosheets, the reductivity of Cr (VI) achieves 99.8% in 15 min under irradiation of 200–800 nm light. At the same time, an in situ Cr (III)-doping occurs spontaneously and triggers pronounced visible light driven photocatalysis, reducing 99% of Cr (VI) in 100 min under irradiation of 400–800 nm light.

Titanium dioxide is a superior photocatalytic material with the conspicuous advantages of high stability and activity, natural abundance, low cost, and nontoxicity.[1] Titanium oxide nanosheets (NS) have attracted prime attention because of the high photocatalytic activities owing to a fully exposed surface making it possible to utilize all surface active sites.[2] In this case, high dispersity is crucial to retain the large surface area with large number reactive sites. For nanosheets, forming large-scale continuous 2D nanostructure favors preventing undesirable layer-by-layer stacking of sheet-like crystallites,

thus retaining the high dispersed state. In addition, for nanosheets with atomic thickness, quantum confinement effects can potentially lead to a significant modification of electronic structures and induce novel physical phenomena.[3] So large-size TiO$_2$ nanosheets, having large side lengths but ultrathin thicknesses, with good monodispersity, should be ideal materials for photocatalysts with high activities.

Synthesis of large-size titanium oxide nanosheets had been a challenging work, until Ti$_{0.87}$O$_2^{0.52-}$ nanosheets with a side length of several tens of micrometers were synthesized through chemical exfoliation to the parent layered K–Ti–Li–O compounds prepared by solid-state calcination at high temperature (≈800 °C).[4] Lately, the synthesis of large-size TiO$_2$ (B) nanosheets by hydrothermal methods was reported.[5] Those remarkable works show us the intriguing optical, photochemical, and electronic properties of titanium oxides nanosheets as well as their improved photocatalytic performance. However, the factors having significant influence on the dispersity of the resultant titanium oxide nanosheets exist in those synthesis approaches. For instance, the hydrothermal treatment, involving relatively high temperature and pressure, could cause agglomeration of the products.[6–8] Exfoliation effects of the parent lamellar crystal determine single-layer or multiple-layer of the resultant nanosheets.[9–12] For nanosheets, agglomerations not only cause considerable loss in surface active sites but also build undesirable surface atoms bonding leading to the loss of the atomic thickness thus losing the potential quantum size effects.[13–15]

In this work, without hydrothermal treatments or chemical exfoliations, we obtained large-size anatase TiO$_2$ nanosheets by the long term aging of precursors in a dilute nitric acid aqueous solution at the low temperature of 4 °C. Owing to the low-temperature ripening and free growth, the resultant TiO$_2$ nanosheets achieved good monodispersity and large-scale continuous 2D nanostructure. Photocatalytic reduction of Cr (VI), one of the major inorganic pollutants in waste water due to their toxicity, bioaccumulation, and persistence,[16] was chosen as the probe reaction to evaluate photocatalytic activities of the anatase TiO$_2$ nanosheets. Owing to the monodispersed large-scale continuous 2D structure, the anatase TiO$_2$ nanosheets demonstrated excellent photocatalytic activities and special surface effects triggering spontaneously visible light (VL) driven photocatalysis.

Prof. X. Tang, J. Lin
School of Science
Chongqing University of Posts and Telecommunications
Chongqing 400065, P. R. China
E-mail: tangxiao@cqupt.edu.cn

Prof. J. Qian, Dr. W. Chu
College of Materials Science and Engineering
Chongqing University
Chongqing 400065, P. R. China

Prof. G. Cao
Materials Science and Engineering
University of Washington
Seattle, WA 98195-2120, USA
E-mail: gzcao@u.washington.edu

The ORCID identification number(s) for the author(s) of this article can be found under https://doi.org/10.1002/smll.201701964.
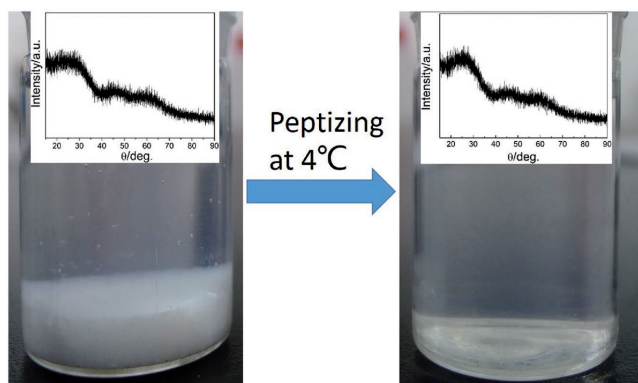
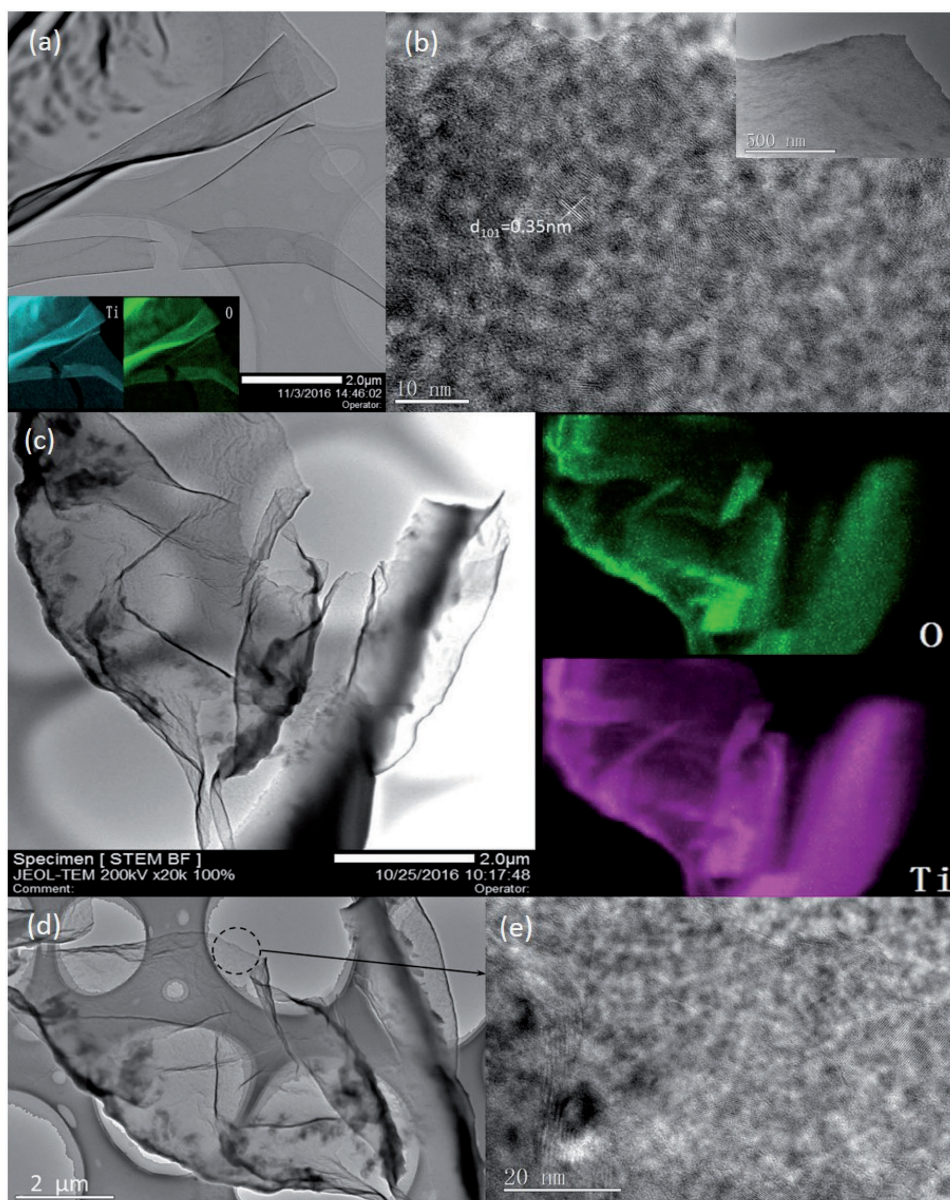**Figure 1.** Peptization of the white precipitation (the hydrolysis product of TBT).

The formation of the large-size anatase TiO_2 nanosheets underwent two phases of peptizing stage (about 7 d) and ripening stage (over 20 d). The precursor is the hydrolysis product of tetrabutyl titanate (TBT) reacting with dilute nitric acid aqueous solution. TBT was dissolved into ethanol to make a uniform mixture serving as the reactant. And then the reactant was dropped into the dilute nitric acid aqueous solution at 2 °C to undergo hydrolysis reaction. In the first stage, the precursor was kept at 4 °C for peptizing. About 7 d later, the white precipitate (the hydrolysate of TBT) peptized into a transparent sol (**Figure 1**). The white precipitate and the transparent sol were freeze-dried into dry samples to undergo X-ray diffraction (XRD) experiments. XRD patterns (the inset of Figure 1) of the two samples show the same bread-shaped diffraction peaks, which indicated that they are amorphous phases with similar microstructure. The TEM image (**Figure 2**a) reveals the morphology of the peptized product to be colloidal nanosheets. The selected area electron diffraction pattern (the inset of Figure 2b) of the sheet-like sample is a diffusion ring, indicating the absence of periodic structure. The high-resolution TEM (HRTEM) image (Figure 2b) shows curving lattice fringes, which reveals that the colloidal nanosheets are formed by atom networks with short-range ordered microstructure.
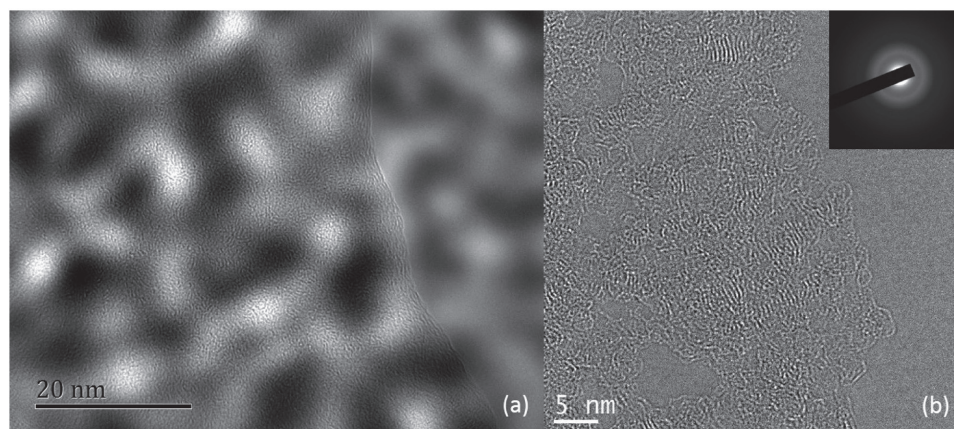
In the second stage, the transparent sol was kept at 4 °C for aging. After 20 d of aging, the sol was still transparent. The stereomorphology of the product was clearly evidenced by TEM in scanning mode (STEM). **Figure 3**a shows the STEM and energy dispersive X-ray (EDS) element mapping images. It can be seen that the 20 d aging product is large-size colloidal nanosheets and the edges roll up due to surface tension. The EDS element mapping results (the inset of Figure 3a) illustrate the uniform distribution of Ti and O atoms in the nanosheets. The TEM image (the inset of Figure 3b) reveals a continuous spongy structure of the colloidal nanosheets. The HRTEM image (Figure 3b) demonstrated that small sized lattices with the fringe spacing of 0.35 nm, corresponding to (101) crystal facet of anatase TiO_2, have begun to grow on the colloidal nanosheets. Keep aging at 4 °C for 5 months, the sol stayed transparently. The STEM image and the corresponding element mapping were given in Figure 3c, which revealed a stable TiO_2 nanosheets with uniform distribution of Ti and O atoms and estimated side length over 10 µm. Comparing with the 20 d aging product, the 5 month aging one is much thinner and more flexible. The high-magnification image (Figure 3e) of the selected part on the TEM image (Figure 3d) shows transparent nanosheets with well-defined lattice fringes, indicating better ripening of the product. HRTEM images (Figure S1a, Supporting Information) and XRD patterns (Figure S1b, Supporting Information) demonstrated the microstructure evolution of the product from peptizing to ripening stage. It was evidenced that TiO_2, ripened in the aqueous solution at the low temperature of ≈4 °C, would undergo a special microstructure evolution, from the initial aperiodic atom-networks, gradually growing into low crystallized continuous spongy structure with small crystal facets, and ultimately forming large-size anatase nanosheets. In addition, the diffraction peaks on XRD patterns (Figure S1b, Supporting Information) are broad and short, indicating the small size of the corresponding crystal planes. Given the large size of the TiO_2 nanosheets, the 5 month aging TiO_2 nanosheets should be polycrystalline phases.

X-ray photoelectron spectroscopy (XPS) signals disclosed the chemical states of Ti and O elements distributed on the surface of the samples in different aging time (7 d, 20 d, and 5 months) (Figure S2, Supporting Information). XPS spectra of all the

Figure 2. a) TEM and b) HRTEM images of the peptized product, amorphous TiO_2 nanosheets, dried.

**ADVANCED
SCIENCE NEWS**
www.advancedsciencenews.com

NANO · MICRO
small
www.small-journal.com

Figure 3. a) STEM and EDS element mapping images and b) HRTEM and TEM images of the 20 d aging product, anatase TiO$_2$ nanosheets, dried; c) STEM and EDS element mapping images, d) low-magnification-TEM image and e) high-magnification-TEM image of the 5 month aging product, anatase TiO$_2$ nanosheets, dried.

samples show that the chemical state of Ti is Ti^{4+},[17,18] while O has two binding states of surface lattice oxygen (O$_L$) and surface Ti—OH group (O$_{OH}$).[19–21] Since the hydrolysate of TBT is the polymer of [Ti—OH]$_n$,[22] the white precipitate should only have Ti—OH but no Ti—O$_L$. However, the peptized product possessed high content of Ti—O$_L$ comparable to Ti—OH, indicating considerable Ti—O$_L$ formed during peptizing. By crystallization, the content of surface Ti—OH group decreased with that of Ti—O$_L$ increasing. In the ripened anatase TiO$_2$ nanosheets, Ti—OH reduced to a small content but not disappeared. It seems that Ti—OH groups play an important role during the formation of the TiO$_2$ nanosheets. It was assumed that the hydrolysate of TBT peptized into highly dispersed ultrasmall
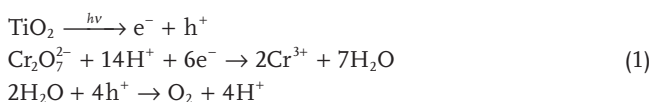
atomic clusters, on the surface of which Ti atoms were bonded with both O$_{OH}$ and O$_L$. Between the two clusters, H (from Ti—OH of one cluster) could form a hydrogen bond with O (from Ti—O of another cluster) in the way of Ti—O:H—O—Ti. Consequently, the ultrasmall atomic clusters interconnected into networks. By Fourier transform infra-red spectroscopy, the active hydrogens, which were available to form hydrogen bonds, in Ti—OH groups were observed in the hydrolysate of TBT hydrolyzed in the dilute nitric acid aqueous solution (Figure S3, Supporting Information). When the product was ripened in the aqueous solution with temperature close to 0 °C, the molecular thermal motions of the system were in a low level, in favor of keeping the linkage of Ti—O:H—O—Ti. As the interconnected
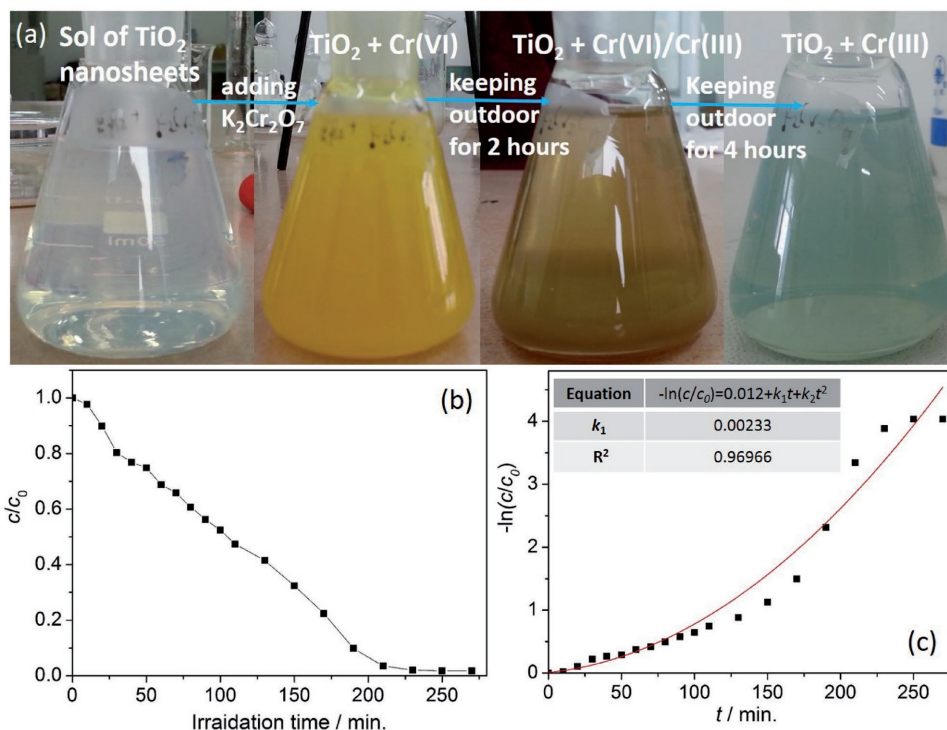
Figure 4. a) Pictures of photocatalytic reduction of Cr (VI) to Cr (III) by the TiO_2 nanosheets under irradiation of natural sunlight; b) photocatalytic reduction of Cr (VI) by the TiO_2 nanosheets under the irradiation of natural sunlight; c) the corresponding reaction kinetics. The second-order equation in the table described the dependence of $-\ln(c/c_0)$ on time (t). Where c is the concentration of Cr (VI) at time t, c_0 is the initial concentration of Cr (VI).
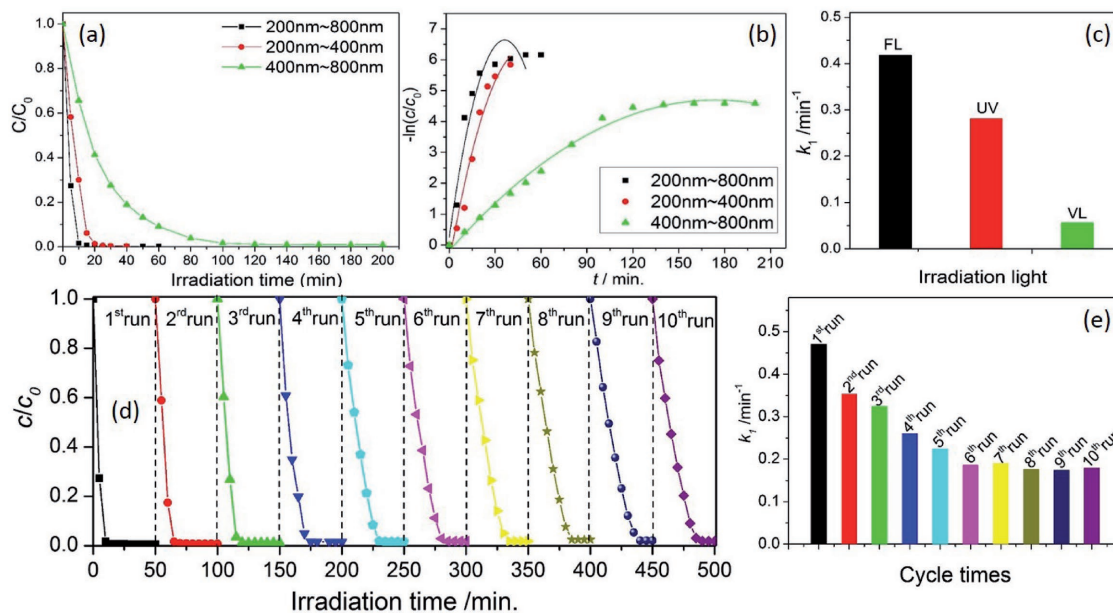
atomic clusters grew into crystallites, the colloid nanosheets with continuous spongy structure formed. Keep ripening in the low temperature aqueous solution, the crystal lattices in the colloidal nanosheets began to extend to form large crystallized regions, while some of the Ti−O:H−O−Ti linker groups were left and entered the lattice to maintain the sheet-like structure. Therefore, the binding energy of O_{OH} in the well crystallized nanosheets differed from those in the amorphous and low crystallized ones (Figure S2, Supporting Information). In addition, the chemical binding strength of Ti−OH differed from that of Ti−O, thus the crystallized TiO_2 nanosheets were flexible. As hydrogen bonds are intermolecular forces, significant thermodynamic fluctuations could destroy them. Therefore, as for hydrothermal ripening systems, small-size nanosheets[23] and nanoparticles (NP)[24] are normally obtained, instead of large-size nanosheets.

Photocatalytic reduction of Cr (VI) to Cr (III) was used as a probe reaction to evaluate photocatalytic activities of the large-size anatase TiO_2 nanosheets. The photocatalytic reduction was performed at 25 ± T °C. A mixture of 50 ml TiO_2 sol (2.34 g dm^{-3}) and 0.1 ml of potassium dichromate ($K_2Cr_2O_7$) aqueous solution (20 g dm^{-3}) served as the reacting system. The pH values of the reacting systems were adjusted with HNO_3 to 2.[25] The typical reactions for photocatalytic reductions of $K_2Cr_2O_7$ by TiO_2 are generally considered as following[26]

$$TiO_2 \xrightarrow{h\nu} e^- + h^+$$
$$Cr_2O_7^{2-} + 14H^+ + 6e^- \rightarrow 2Cr^{3+} + 7H_2O \tag{1}$$
$$2H_2O + 4h^+ \rightarrow O_2 + 4H^+$$

Figure 4a demonstrated the changes of the reacting system under irradiation of outdoor natural sunlight. After 4 h of sunlight irradiation, owing to reduction of Cr (VI) to Cr (III), the yellow suspension changed into a green sol. Photocatalytic reduction of Cr (VI) by NS under the irradiation of natural sunlight and the corresponding reaction kinetics data were given in Figure 4b,c. It demonstrated that 98.3% Cr (VI) was reduced in 230 min. A reaction rate constant $k_1 = 0.00233$ was obtained from the fitting reaction kinetic equation (the correlation coefficient $R^2 > 0.96$) shown in the insert table of Figure 4c. It was intriguing that intrinsic TiO_2, with wide bandgap over 3.2 eV, demonstrated noticeable photocatalytic activity under irradiation of natural sun light.

For accurate evaluation of the photocatalytic reduction capability of NS, the reduction data of Cr (VI) under irradiation of light with different wavelength ranges afforded by a 300W Xenon lamp were compared, as shown in **Figure 5**a–c. NS demonstrated high photocatalytic activities, reducing 99.8% Cr (VI) in 15 min under irradiation of 200–800 nm light full wavelength lights (FL), while it took 25 min to achieve 99.8% Cr (VI) reduction under irradiation of 200–400 nm light (UV). It was noticeable that under irradiation of 400–800 nm VL, cutting off >98% of light with wavelength less than 400 nm with a UV filter, 99% of Cr (VI) was still reduced to Cr (III) in 100 min. The maximum reaction rate constant $k_1 = 0.418$ of Cr (VI) reduction was obtained under FL irradiation. Cutting off visible light, under irradiation of UV light, k_1 decreased to 0.218. Cutting off UV, under irradiation of visible light, the minimum $k_1 = 0.056$ was obtained. It turns out that the NS system has extra

ADVANCED
SCIENCE NEWS
www.advancedsciencenews.com

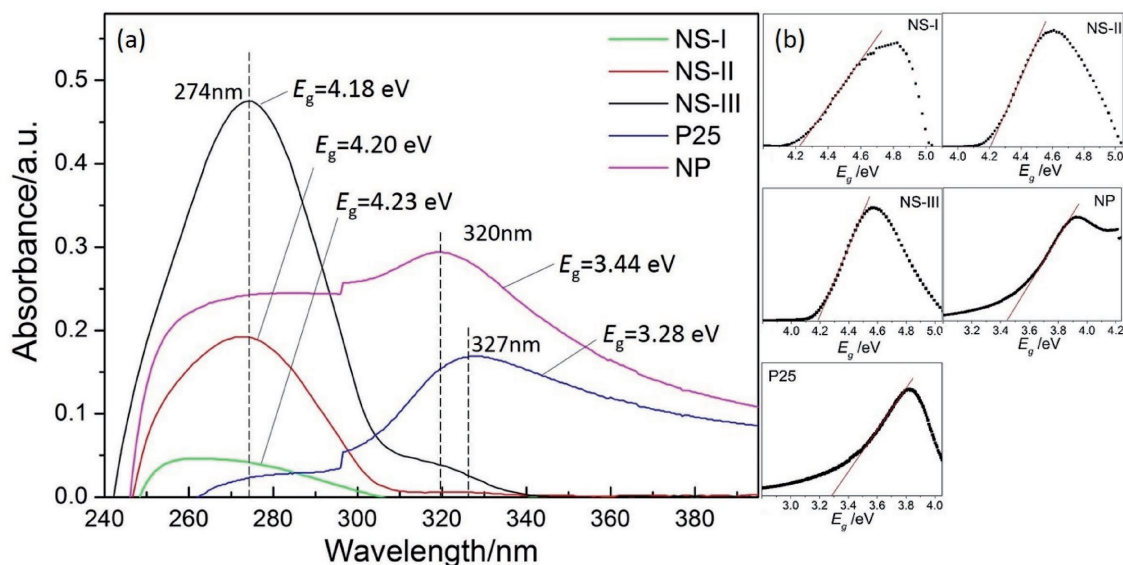NANO MICRO
small
www.small-journal.com

Figure 5. a) Photocatalytic reduction of Cr (VI) by NS under irradiation of 200–800 nm light (FL), 200–400 nm light (UV) and 400–800 nm light (VL); (b) the corresponding reaction kinetics and (c) Cr (VI) reduction rates; (d) reusability of NS for the cyclic degradation of Cr (VI) and (e) Cr (VI) reduction rates under FL irradiation.

response to the light over 400 nm. The reusability of NS for the cyclic photocatalytic reduction of Cr (VI) was tested under FL irradiation. The data were given in Figure 5d,e. For each reduction cycle, one dose of 0.1 ml $K_2Cr_2O_7$ solution (20 g dm^{-3}) was added into the initial 50 ml TiO_2 sol (2.34 g dm^{-3}). The Cr (VI) reduction rate decreased slightly with the cycle times increasing and stabilized after the fourth run. The degradation percentage of Cr (VI) was still up to 99% after the tenth cyclic reduction, indicating the highly efficient and stable photocatalytic reduction performance of NS.

The light absorption properties of TiO_2 were analyzed to obtain some explanation to the high photocatalytic activity of NS. The data of two kinds of TiO_2 nanoparticles, i.e., 200 °C-15-h-hydrothermal treatment anatase TiO_2 NP and commercial Degussa P25, were also given for comparison. In order to capture the highest disperse state, the concentration of TiO_2 in sol was adjusted to a low level to undergo UV–vis absorption spectra investigation. UV–vis absorption spectra revealed the different disperse states of NS, NP, and P25 in their sols (**Figure 6**a). The characteristic absorption peak of NS is located at 274 nm wavelength and the peak is nearly symmetric indicating NS has a uniform microstructure, i.e., monodispersed nanosheets. Comparatively, NP shows an absorption band with a peak at 320 nm and P25 has an asymmetric absorption peak at 327 nm, which associates to the wide size-distribution of nanoparticles. Referring to the typical UV–vis absorption spectra of $Ti_{0.91}O_2^{0.36-}$ nanosheets with the thickness of 0.7 nm, which exhibited similar absorption spectra with an absorption peak at ≈265 nm,[27] the thickness of NS was estimated in the same level. Based on the Tauc plots (Figure 5b), the optical gap energy (E_g) of NSs, decreasing from 4.23 to 4.18 eV by crystallization. And the E_g value of P25 was 3.28 eV and that of NP was 3.44 eV. This

difference originated from their different optical absorption spectra. When underwent UV–vis absorption spectra investigations, the P25 system was just P25 powder (mainly anatase TiO_2 nanoparticles with size of ≈30 nm) solved in the dilute nitric acid aqueous solution, therefore the E_g was close to the value of bulk anatase TiO_2 (3.2 eV). On the other hand, there were other organic solvents, such as ethanol, in the NP system and NS system. As well known, solvent molecules have impact on the optical absorption spectra of the active materials, even though they themselves do not absorb the incident light. This may lead to shifting of the position of absorption peaks, and thus the optical gap energy deviate from the standard 3.2 eV. However, TiO_2 has a relatively small exciton radius (≈1 nm),[28] and thus, for TiO_2 nanoparticles with diameter larger than 1 nm, no appreciable quantum confinement effect, thus no pronounced energy-gap-widening, should be observed.[29] Therefore, the E_g value of NP should be calibrated to 3.2 eV with −0.24 eV. The E_g value of NS should be calibrated with −0.24 eV too. The precursor used to synthesize NP was the transparent sol obtained on the peptizing stage during the synthesis of NS. Instead of 4 °C-5 month ripening, the peptized sol underwent 200 °C-15 h hydrothermal treatment. As a result, the anatase TiO_2 nanoparticles with size of 5–20 nm were obtained. In other words, the chemical composition of the NS system and NP system are the same. Therefore, it was reasonable to use the same value of −0.24eV to calibrate the optical gap energy of NS to 3.94 eV, which was significantly wider than that of bulk anatase TiO_2. The increased bandgap value of 3.85 eV, estimated from the photocurrent action spectra, was also observed in $Ti_{0.91}O_2^{0.36-}$ nanosheets with thickness of 0.7 nm.[30] In addition, a cluster of anatase-like TiO_2 with a diameter of 0.79 nm[31] has a calculated electronic gap of 4.83 eV.[32] Therefore, the thickness of NS should be

ADVANCED
SCIENCE NEWS
www.advancedsciencenews.com

NANO · MICRO
small
www.small-journal.com

Figure 6. a) UV–vis absorption spectra and b) Tauc plots of NS-I (the amorphous colloidal nanosheets), NS-II (20 d aging colloidal nanosheets), NS-III (the 5 month aging anatase nanosheets), NP and P25. When the morphology of TiO$_2$ evolves from (NS-I) to (NS-III), the light absorption increases and forms a significant absorption peak at 274 nm.
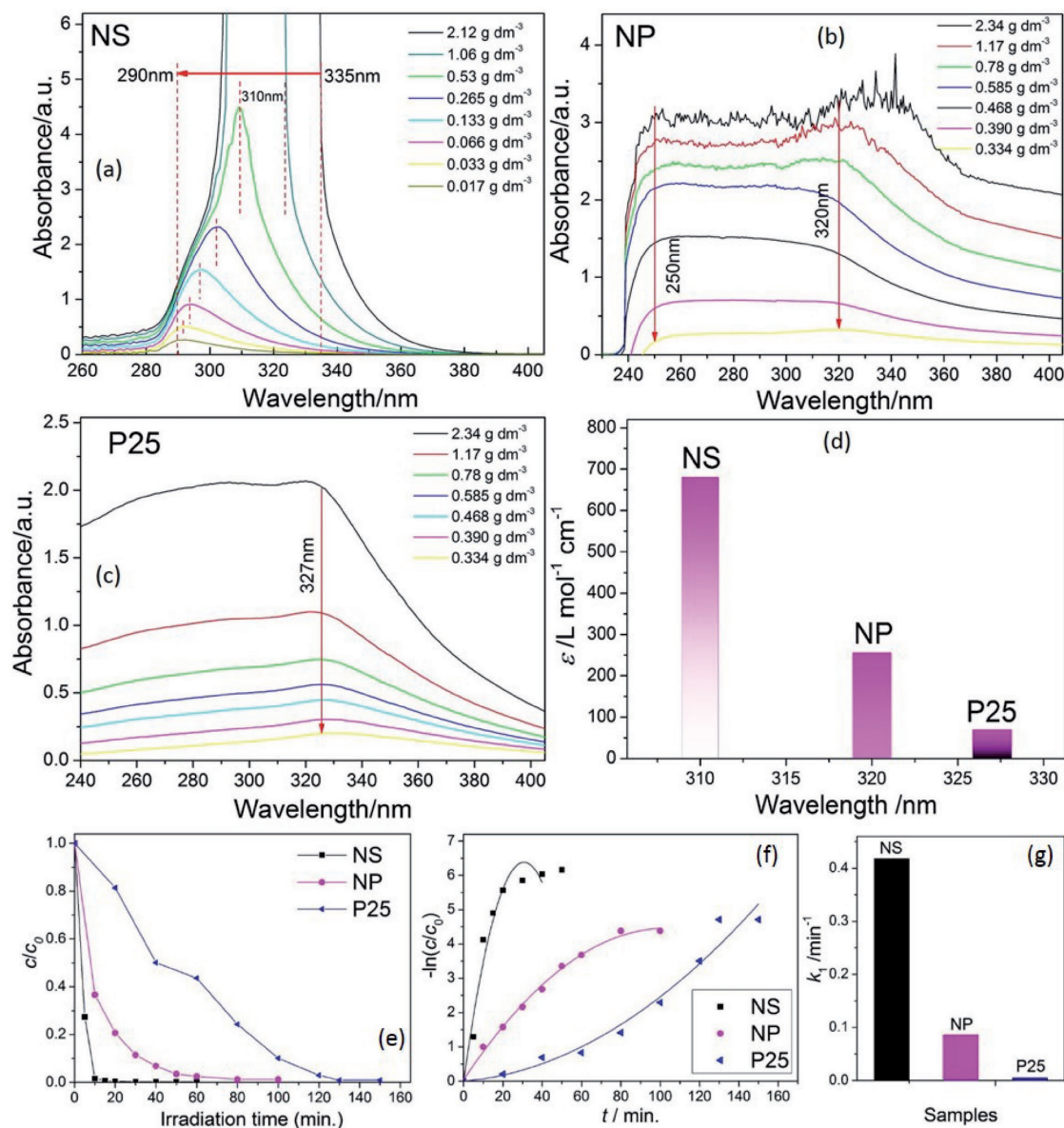
smaller than 1 nm so that an appreciable gap-energy-widening occurred due to quantum confinement effects.

The increased bandgap energy results in the optical absorption of NS shifting to the light less than 300 nm, which is undesirable to the sunlight driven photocatalysis. However, in the NS sol with high TiO$_2$-concentration (2.12 g dm^{-3} for instance), the optical absorption edges of 335 nm was observed. Diluting the sol, the optical absorption peak shifted back to the wavelength less than 300 nm (**Figure 7**a). This behavior was not observed in the diluted NP or P25 sol, the optical absorption peaks of which did not shift but only descended due to absorbance decreasing (Figure 7b,c). This TiO$_2$-concentration related optical absorption peaks shifting indicates the low-temperature-ripening indeed prevents the agglomeration of TiO$_2$ nanosheets. And the optical properties of NS could be modified by simply changing the concentration of TiO$_2$. As a result, NSs, with the characteristic optical bandgap of 3.94 eV, demonstrated photocatalytic activities under irradiation of sunlight.

In addition, the optical absorption capacity of NS was significantly higher than those of NP and P25. Maximum molar extinction coefficients ε (L mol^{-1} cm^{-1}) of NS, NP, and P25 to UV (over 300 nm) were given in Figure 7d. The ε of NS (680.6 L mol^{-1} cm^{-1}) is nearly one order of magnitude higher than that of P25 (69.6 L mol^{-1} cm^{-1}) and 2.5 times higher than that of NP (256.0 L mol^{-1} cm^{-1}). Similarly, the colloidal suspension of Ti$_{0.91}$O$_2^{0.36-}$ nanosheets shows pronounced UV absorption with the mole extinction coefficient two orders of magnitude higher than that of the bulk TiO$_2$.[33] Comparing the photocatalytic reduction data of NS, NP, and P25 (Figure 7e–g), it can be seen that under FL irradiation, NS, reducing 99.8% Cr (VI) in 15 min, demonstrate much higher photocatalytic activity than NP and P25, the data of which were 80 min/98.7% and 130 min/99.0%, respectively. The fitting reaction kinetics results indicate that the Cr (VI) reduction rate of NS is nearly

two orders of magnitude higher than that of P25 and about five times higher than that of NP.

High absorption capacity to UV results in high photocatalytic activity of NS under irradiation of FL or UV, whereas cannot explain the extra response of NS to the light with wavelength over 400 nm (VL). To figure this out, after Cr (VI) was reduced to Cr (III) by NS under UV irradiation, the UV–vis absorption spectra of the resultant green sol was examined and compared with that of NS (**Figure 8**a). The product of Cr (VI) reduction is Cr (III), corresponding to the absorption peak at 575 nm, thus the sol turns into green. It was noticeable that there was another significant optical absorption between 400 and 500 nm on the spectra, which revealed a modification of electronic structure of TiO$_2$. The Tauc plot in the set of Figure 7a shows the E_g of NS decreases to 2.8 eV, which indicates that there is an impurity energy level in the bandgap of TiO$_2$. Two potential situations of oxygen vacancies (corresponding to Ti^{3+}) and Cr (III)-doping were considered to be associated to the impurity energy level. To figure this out, the green sol was freeze-dried (Figure 8b) to undergo XPS characterization. The bind energy of Ti^{3+} 2p$_{3/2}$ is 457.4 eV, whereas the Ti 2p$_{3/2}$ spectra only show the peak at 458.9 eV corresponding to Ti^{4+} 2p$_{3/2}$ (Figure 8c), indicating free of surface oxygen vacancies. On the other hand, the fitted Cr 2p$_{3/2}$ spectra shows a peak at 576.7 eV (Figure 8d) corresponding to the bind energy of Cr^{3+} in chemical binding with O.[34] In view of the similar ionic radii of Ti^{4+} (0.068 nm) and Cr^{3+} (0.064 nm), Cr^{3+} could replace Ti^{4+} in surface lattice of NS and formed an impurity energy level in the forbidden band of TiO$_2$. Referring to the calculations on the electronic structure of Cr-doped TiO$_2$, the occupied Cr^{3+} is ≈1.0 eV higher than the valence band top of TiO$_2$. Therefore, Cr (III)-doped TiO$_2$ shows an optical absorption around 400–500 nm,[35–37] which is in well agreement with our results. Considering three valence electrons of Cr^{3+}, if Ti atoms were replaced by Cr^{3+}, it should form an acceptor state closing to the valence band of TiO$_2$. Therefore,

ADVANCED
SCIENCE NEWS
www.advancedsciencenews.com

NANO·MICRO
small
www.small-journal.com

Figure 7. Absorption spectra of diluted systems of a) NS, b) NP, and c) P25; d) maximum molar extinction coefficients ε (L mol^{-1} cm^{-1}) of NS, NP, and P25 to UV; e) photocatalytic reduction of Cr (VI) by NS, NP, and P25 under irradiation of FL; f) the corresponding reaction kinetics and g) Cr(VI) reduction rates.

the conduction band of Cr (III)-doped NS would not have a substantial change, while the valence band edge should have an extension into the forbidden band, causing the bandgap energy of 3.94 eV decreasing by 1.14–2.8 eV, thus extended the optical absorption into 400–500 nm range. It was evidenced that during Cr (VI) reduction, in situ Cr (III)-doping in NS occurred at room temperature and triggered the visible light driven photocatalysis. Actually, the so-called low-temperature-doping effects were also observed in TiO$_2$ (B) nanosheets, which achieved I-doping at the temperature ≈100 °C.[38] The schematic illustration of the evolution of the energy band structure in the situations of low TiO$_2$-concentration, high TiO$_2$-concentration and Cr (III)-doping (Figure S4, Supporting Information) explained the response of the NS system to visible light. When

TiO$_2$-concentration in a low level, the optical bandgap of NS was 3.94 eV. Increasing the TiO$_2$-concentration resulted in the absorption peak red-shift to 310 nm, corresponding smaller bandgap of 3.60 eV. By Cr (III)-doping, the optical bandgap of NS was further narrowed to 2.8 eV.

In summary, we discovered a special microstructure evolution of TiO$_2$ in aqueous solution at the low temperature of ≈4 °C, which is from aperiodic atomic networks gradually growing into well crystallized anatase nanosheets. Based on this experimental finding, we have synthesized large-size anatase TiO$_2$ NS with good monodispersity and appreciable size-base quantum effects. Owing to the monodisperse large-scale 2D nanostructure, NS exhibited three aspects of special properties: (1) the concentration related optical absorption
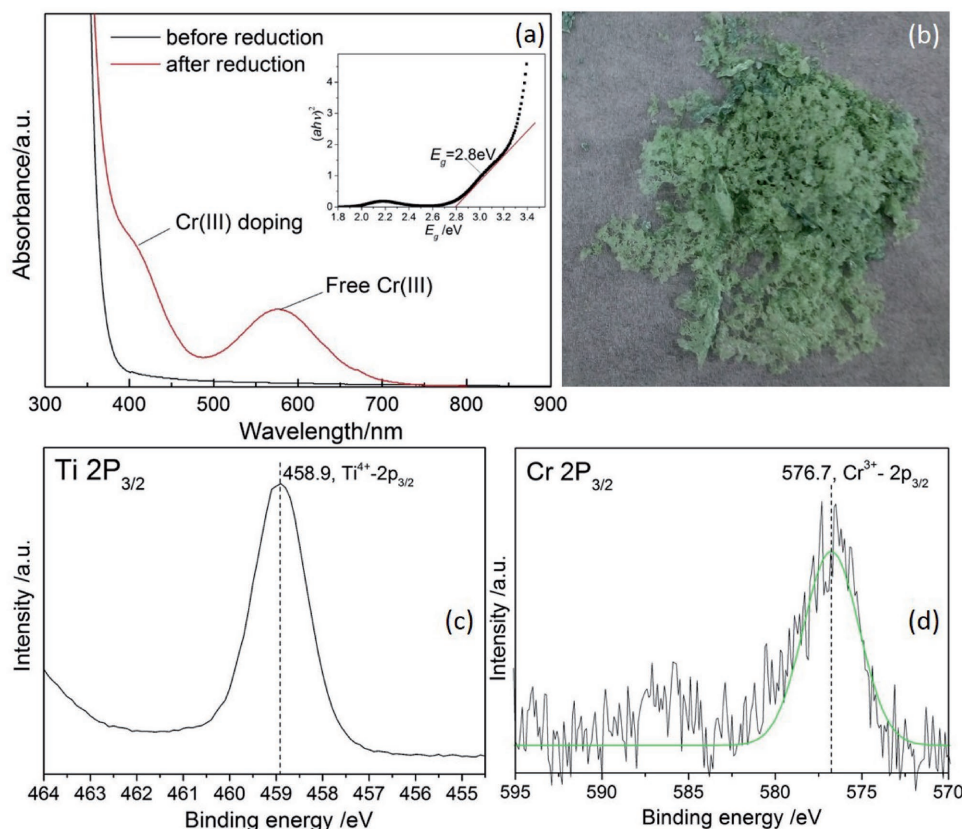
Figure 8. a) Comparison of UV–vis absorption spectra of NS before and after Cr (VI) reduction under irradiation of UV; b) pictures and (c, d) XPS spectra of the freeze dried NS after Cr (VI) reduction.

peaks shifting; (2) the high optical absorption capacity; (3) the low temperature doping effect. As a result, NS demonstrated high photocatalytic activities of reducing 99.8% Cr (VI) in 15 min under irradiation of 200–800 nm light and the degradation percentage of Cr (VI) was still up to 99% after ten cyclic reductions. During Cr (VI) reduction, an in situ Cr (III)-doping occurred spontaneously, which triggered visible light driven photocatalysis of NS, achieving 98.3% of Cr (VI) reduction at irradiation of natural sunlight. The results demonstrated here may help to the development of highly active TiO_2 nanosheets for energy and environment related applications.

Supporting Information

Supporting Information is available from the Wiley Online Library or from the author.

Acknowledgements

Conflict of Interest

The authors declare no conflict of interest.

Keywords

[1] H. Lin, X. Wang, *Adv. Funct. Mater.* **2016**, *26*, 1580.
[2] S. Selcuk, A. Selloni, *Nat. Mater.* **2016**, *20*, 1.
[3] E. C. Tyo, S. Vajda, *Nat. Nanotechnol.* **2015**, *10*, 577.
[4] T. Sasaki, Y. Evina, T. Tanaka, T. Tanaka, M. Harada, M. Watanabe, G. Decher, *Chem. Mater.* **2001**, *13*, 4661.
[5] G. L. Xiang, T. Li, J. Zhuang, X. Wang, *Chem. Commun.* **2010**, *46*, 6801.
[6] S. Liu, H. Jia, L. Han, J. Wang, P. Gao, D. Xu, J. Yang, S. Che, *Adv. Mater.* **2012**, *24*, 3201.
[7] S. H. Ahn, D. J. Kim, W. S. Chi, J. H. Kim, *Adv. Mater.* **2013**, *25*, 4893.
[8] H. M. Ghaithana, S. M.H. Qaida, M. Hezam, J. P. Labisb, M. Alduraibia, I. M. Bedjaf, A. S. Aldwayyana, *Electrochim. Acta* **2016**, *212*, 992.
[9] T. Tanaka, Y. Ebina, K. Takada, K. Kurashima, T. Sasake, *Chem. Mater.* **2003**, *15*, 3564.
[10] N. Sakai, Y. Ebina, K. Takada, T. Sasaki, *J. Am. Chem. Soc.* **2004**, *126*, 5851.
[11] T. Orzali, M. Casarin, G. Granozzi, M. Sambi, A. Vittadini, *Phys. Rev. Lett.* **2006**, *97*, 156101.

[12] K. Fukuda, Y. Ebina, T. Shibata, T. Aizawa, I. Nakai, T. Sasaki, *J. Am. Chem. Soc.* **2007**, *129*, 202.

[13] H. Wang, H. Feng, J. Li, *Small* **2014**, *10*, 2165.

[14] W. Yang, J. Li, Y. Wang, F. Zhu, W. Shi, F. Wan, D. Xu, *Chem. Commun.* **2011**, *47*, 1809.

[15] C. Hu, X. Zhang, X. H. Li, Y. Yan, G. Xi, H. Yang, H. Bai, *Chem. Eur. J.* **2014**, *20*, 13557.

[16] C. E. Barrera-Díaz, V. Lugo-Lugo, B. Bilyeu. *J. Hazard Mater.* **2012**, *223–224*, 1.

[17] J. M. Cai, Y. M. Zhu, D. S. Liu, M. Meng, Z. P. Hu, Z. Jiang, D. Zhang, S. Xiao, X. Li, G.C Li, *ACS Catal.* **2015**, *5*, 1708.

[18] Z. Lian, P. Xu, W. Wang, T. Koppe, D. Wang, T. Andreu, G. Chen, U. Vetter, *ACS Appl. Mater. Interfaces* **2015**, *7*, 4533.

[19] Y. Yan, M. Han, A. Konkin, T. Koppe, D. Wang, T. Andreu, G. Chen, U. Vetter, J. R. Morante, P. Schaaf, *J. Mater. Chem. A* **2014**, *2*, 12708.

[20] W. Zhou, W. Li, J. Q. Wang, Y. Qu, Y. Yang, Y. Xie, K. F. Zhang, L. Wang, H. G. Fu, D. Y. Zhao, *J. Am. Chem. Soc.* **2014**, *136*, 9280.

[21] G. Wang, H. Wang, Y. Ling, Y. Tang, X. Yang, R. C. Fitzmorris, C. Wang, J. Z. Zhang, Y. Li, *Nano Lett.* **2011**, *11*, 3026.

[22] Y. Shaban, M. Sayed, A. Maradny, *Chemosphere* **2013**, *91*, 307.

[23] L. Etgar, W. Zhang, S. Gabriel, S. G. Hickey, M. K. Nazeeruddin, A. Eychmüller, B. Liu, M. Grätzel, *Adv. Mater.* **2012**, *24*, 2202.

[24] J. S. Lee, K. H. You, C. B. Park, *Adv. Mater.* **2012**, *24*, 1084.

[25] D. Lu, W. Chai, M. Yang, P. Fang, W. Wu, B. Zhao, R. Xiong, H. Wang, *Appl. Catal., B* **2016**, *190*, 44.

[26] W. Yan, Q. Chen, X. Meng, B. Wang, *Sci. China Mater.* **2017**, *60*, 449.

[27] R. Ma, T. Sasaki, *Adv. Mater.* **2010**, *22*, 5082.

[28] N. Serpone, D. Lawless, R. Khairutdinov, *J. Phys. Chem.* **1995**, *99*, 16646.

[29] M. J. Llansola-Portoles, J. J. Bergkamp, D. Finkelstein-Shapiro, *J. Phys. Chem. A* **2014**, *118*, 10631.

[30] N. Sakai, Y. Ebina, K. Takada, *J. Am, Chem. Soc.* **2004**, *126*, 5851.

[31] A. Iacomino, G. Cantele, D. Ninno, I. Marri, S. Ossicini, *Phys. Rev. B* **2008**, *78*, 075405.

[32] L. Chiodo, M. Salazar, A. H. Romero, S. Laricchia, F. D. Sala, A. Rubio, *J. Chem. Phys.* **2011**, *135*, 44704.

[33] N. Sasaki, M. Watanabe, *J. Phys. Chem. B* **1997**, *101*, 10159.

[34] I. Serafin, A. Kotarba, M. Grzywa, Z. Sojka, *J. Catal.* **2006**, *239*, 137.

[35] H. Li, S. Yin, Y. Wang, T. Sekino, S. W. Lee, T. Sato, *J. Catal.* **2013**, *297*, 65.

[36] H. Irie, T. Shibanuma, K. Kamiya, S. Miura, T. Yokoyama, K. Hashimoto, *Appl. Catal., B* **2010**, *96*, 142.

[37] J. Wang, S. Yin, T. Sato, *J. Photochem. Photobiol. A* **2007**, *187*, 72.

[38] G. L. Xiang, Y. G. Wang, D. Wu, *Chem. Eur. J.* **2012**, *18*, 4759.